Spring 2015

External Electric Fields: A New Tool for Controlling Ultracold Polar Molecules

Jamie Shaw
Jamie.Shaw@Colorado.EDU

External Electric Fields: A New Tool for Controlling Ultracold Polar Molecules

by

J. C. Shaw

A thesis submitted to the

Faculty of Physics of the

University of Colorado in partial fulfillment

of the requirements for graduating with Honors

Bachelor of Arts

Department of Physics

2015

This thesis entitled:
External Electric Fields: A New Tool for Controlling Ultracold Polar Molecules
written by J. C. Shaw
has been approved for the Department of Physics

Thesis Advisor: Deborah S. Jin
Department of Physics

Prof. James K. Thompson
Department of Physics

Prof. Carl Lineberger
Department of Chemistry and Biochemistry

Date _____

The final copy of this thesis has been examined by the signatories, and we find that both the content and the form meet acceptable presentation standards of scholarly work in the above mentioned discipline.

Shaw, J. C. (B.A., Physics)

External Electric Fields: A New Tool for Controlling Ultracold Polar Molecules

Thesis directed by Prof. Deborah S. Jin

Ultracold dipolar molecules present many new and novel properties for studying the quantum dynamics of many-body physics. In particular, large electric dipole moments found in polar molecules can be tuned with external electric fields which provide for precise control over dipole-dipole interactions. JILA's second generation ultracold KRb molecule experiment provides new capabilities for applying external electric fields. Generating these fields requires several stable high-voltage sources in order to precisely control the transitions in ultracold dipolar molecules. This thesis will discuss my work towards creating stable high-voltage sources to be used in the second generation KRb apparatus.

Acknowledgements

I would like to thank both of my brilliant advisors, Debbie and Jun, for providing me with the opportunity to work on this project. Their ability to understand concepts in the simplest and most elegant ways never ceases to amaze me. I have been extremely lucky to work with them and will always remember this experience. I would also like to thank my graduate student mentor, Steven Moses, and graduate student, Jake Covey, for being patient with me through all the difficulties I encountered in striving to understand the KRb experiment. I also have Terry Brown, in JILA's electronics shop, to thank for the time he spent with me explaining the fine details of the circuitry used for my project. Ultimately, I would not have completed this thesis had it not been for my incredible friends at both CU Boulder and NH supporting me with their many words of encouragement. I am extremely grateful to have had the opportunity to work on JILA's ultracold KRb molecule experiment.

Contents

Chapter

Figures

Figure

Chapter 1

Introduction

1.1 A Brief Background in Ultracold Physics

Over the past three decades, the field of atomic, molecular, and optical physics has been wildly successful in its attempts to bring atoms to a halt. The field has developed several new tools for trapping and cooling atoms that allow for precise control and manipulation of both atoms' internal and external degrees of freedom. This has led to ground-breaking realizations of new and exciting quantum phases of matter predicted nearly a century ago, such as the Bose-Einstein condensate and degenerate Fermi gas [1], [2]. With these realizations has followed considerable interest in studying the physics of many-body quantum systems, which highlight the underlying interactions that make up our macroscopic world. The ability to precisely tune atomic interactions makes the field of ultracold physics an ideal platform for simulating systems found in fields such as condensed matter and high energy physics [3],[4].

The idea to use quantum interactions for simulating system dynamics has led to considerable interest in confining atoms to periodic potentials as a way of mimicking the underlying interactions found in crystalline solids. In condensed matter physics, electrons can be modelled as moving about a landscape of atoms that provide periodic potentials. As a way to mirror this, atoms are trapped in optical lattices created by interfering lasers which provide freedom to tune lattice geometries as well as insulating and conducting band structures [4]. Atoms interact with one another over short distances via contact and spin interactions. These interactions offer a vast range of research opportunities from superconductivity to

quantum computation [4].

1.2 Why Ultracold Polar Molecules?

Despite the large success in the field of ultracold atomic physics, some phenomena remain difficult to replicate using atoms. As a result, considerable focus has since been placed on gaining similar control over simple molecules due to their rich internal energy structure. Molecules are inherently more complex than atoms and present a broader range of tunable parameters useful for exploring the quantum dynamics of many-body physics. This provides various methods for approaching questions in condensed matter physics, quantum information, and precision measurement [5],[6].

A particular interest in ultracold molecules is rooted in the fact that hetero-nuclear molecules possess electric dipole moments allowing them to strongly interact with external electric fields and one another via dipole-dipole forces. One could also use atoms to realize dipole-dipole interactions, however, the interactions between molecules can be several orders of magnitude larger, making polar molecules ideal for studying the effects of long-range anisotropic[1] interactions [7]. This could be important, for example, in simulating quantum magnetism [8].

1.3 A Qualitative Picture

Most are familiar with the concept that electric fields exhibit forces on charged particles. In accordance with this intuition, an atom in the presence of a DC electric field will feel a force that results in a separation of its opposite charges (protons and electrons). Classically speaking, we can picture this as a breaking of symmetry in the distribution of electrons bound to the nucleus resulting in an induced dipole moment. The induced dipole moment

[1] The anisotropy of dipole-dipole interactions means that side-to-side interactions are stronger than head-to-tail.

also causes the energy structure to shift resulting in what is known as the Stark shift.

Similar to an atom, a molecule exposed to a DC electric field will experience an induced dipole moment and corresponding Stark shift. However, in the absence of an electric field, a molecule with a permanent dipole moment will show no dipole. This is an inherent result of the quantum mechanical nature of the microscopic world. Accordingly, in order to observe the exciting associated with dipolar molecules, such as dipole-dipole interactions, it is necessary to provide external electric fields.

1.4 Thesis Outline

The following chapters will provide a quantitative understanding for how electric fields will affect molecules in the second generation KRb experiment in JILA. While the first generation KRb experiment has been tremendously successful over the past $\sim$10 years, limitations in its ability to create electric fields has motivated careful attention to the generation II design. With chapter 2, I hope to present context that is useful for understanding the future requirements for electric fields in our experiment. With a context set, chapter 3 will provide finer details revolving around the features of the second generation apparatus and functions for external electric fields. Following this, chapter 4 will discuss the requirements for future experiments. Finally, as my part in this experiment, chapter 5 will present a design intended to achieve the needs for future experiments, and will ultimately present preliminary data that marks my progress thus far.

Chapter 2

Dipolar Molecules in Electric Fields

2.1 A Quantitative Picture

2.1.1 Stark shift

The Stark shift is the result of the interaction between a permanent dipole moment and an external electric field [9]. Its effect is a shifting of energy levels within an atom or molecule. We can quantify this shift by treating the DC electric field as a first order perturbation to the rotational[2] structure of the KRb molecule. We can consider the molecule's rotation in the $|\mathrm{N},m_N\rangle$ basis, where N describes the rotation of the molecule about the molecular axis and m_N is the projection of the rotational state along the field direction. Unperturbed, the molecules' rotational energy is given by,

$$\langle N, m_N \mid \hat{H}^o \mid N', m'_N \rangle = BN\,(N+1)\,\delta_{N,N'}\delta_{m_N,m'_N} \tag{2.1}$$

where B is the rotational constant for $^{40}K^{87}Rb$ in energy units and h is Planck's constant. Turning on an external electric field provides a first order perturbation,

$$\langle N, m_N \mid \hat{H}^1 \mid N', m'_N \rangle = - d \cdot \varepsilon \sqrt{(2N+1)\,(2N'+1)}\,(-1)^{m_N} \begin{pmatrix} N & 1 & N' \\ -m_N & 0 & m'_N \end{pmatrix} \begin{pmatrix} N & 1 & N' \\ 0 & 0 & 0 \end{pmatrix} \tag{2.2}$$

[2] We choose to examine rotational states as they provide the lowest energy degree of freedom in our molecules, can be easily excited by microwave frequencies, and as will be considered later on, provide strong interactions mediated by dipole-dipole forces.

where d is the permanent electric dipole moment of KRb and ε is the magnitude of the external electric field. The three-j symbols ensure that states with the same m_N are mixed by the electric field while |N,m_N⟩ and |N,$-m_N$⟩ remain degenerate [10]. Using this perturbed Hamiltonian we can fill the matrix describing the N=0,1 states, shown in Eqn.2.3. The states are organized starting from H_{11} and moving down the diagonal, |0,0⟩, |1,-1⟩, |1,0⟩, |1,1⟩ respectively.

$$H_{rot} = \begin{pmatrix} 0 & 0 & -\frac{d\cdot\varepsilon}{\sqrt{3}} & 0 \\ 0 & 2B & 0 & 0 \\ -\frac{d\cdot\varepsilon}{\sqrt{3}} & 0 & 2B & 0 \\ 0 & 0 & 0 & 2B \end{pmatrix} \tag{2.3}$$

The non-zero off-diagonal elements indicate that the electric field mixes states of opposite parity and splits the |1,0⟩ state from other degenerate states in the triplet manifold. The Stark shift is found by diagonalizing the matrix in order to obtain the eigenvalues, shown in Eqn. 2.4 (ordered the same way as above).

$$E_{rot} = \begin{pmatrix} B - \sqrt{B - \frac{(d\cdot\varepsilon)^2}{3}} \\ 2B \\ B + \sqrt{B - \frac{(d\cdot\varepsilon)^2}{3}} \\ 2B \end{pmatrix} \tag{2.4}$$

While not represented by this calculation, the remaining degenerate states are split by the hyperfine interaction due to the magnetic dipole moments of the K and Rb nuclei. These interactions rise to 36 hyperfine levels within the |1,0⟩ state. This results from the possible combinations of projections from the K and Rb nuclei. Considering this, we may represent any state by |N,m_N,m_K,m_{Rb}⟩, where m_K and m_{Rb} are the projections of the nuclear moments on the quantization axis.

Calculating the Stark shift with only the first two rotational levels shows a symmetric splitting between the between states of opposite parity. In reality this does not accurately describe our molecules, since, in principle, there are an infinite number of higher states that mix with the ones discussed here. Realizing it would be impossible and unnecessary to include all states, we can look for convergence of a single state at an arbitrarily large field in order to determine a maximum number of states to include in the calculation. To do this, we put energy in units of rotational constant, B, and write ε in terms of the critical electric field, $\frac{\varepsilon}{\varepsilon_o}=\frac{d\cdot\varepsilon}{Bh}$. Using the ground rotational state evaluated at 1MV/cm we find that the Stark shifted value converges around N_{max} equal to 7 or 8, as shown in Figure 2.1. With this we choose to include 8 states.

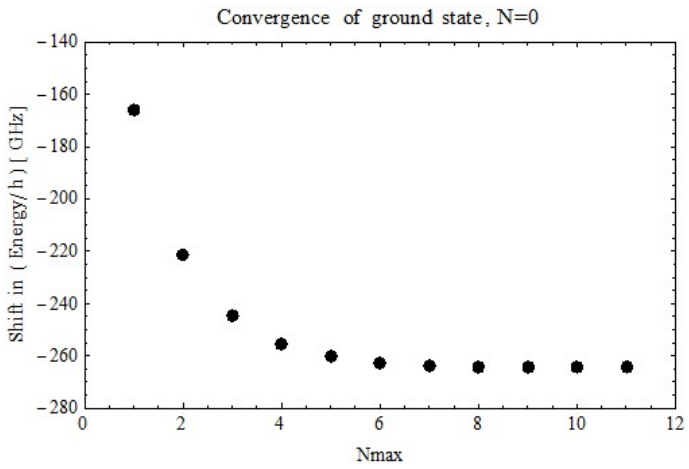

Figure 2.1: Convergence of $|\mathrm{N},m_N\rangle$ Stark shift considering higher numbers of states.

Below, Figure 2.2 shows the Stark shift of the first two rotational states in KRb and demonstrates the effect of mixing with higher states.

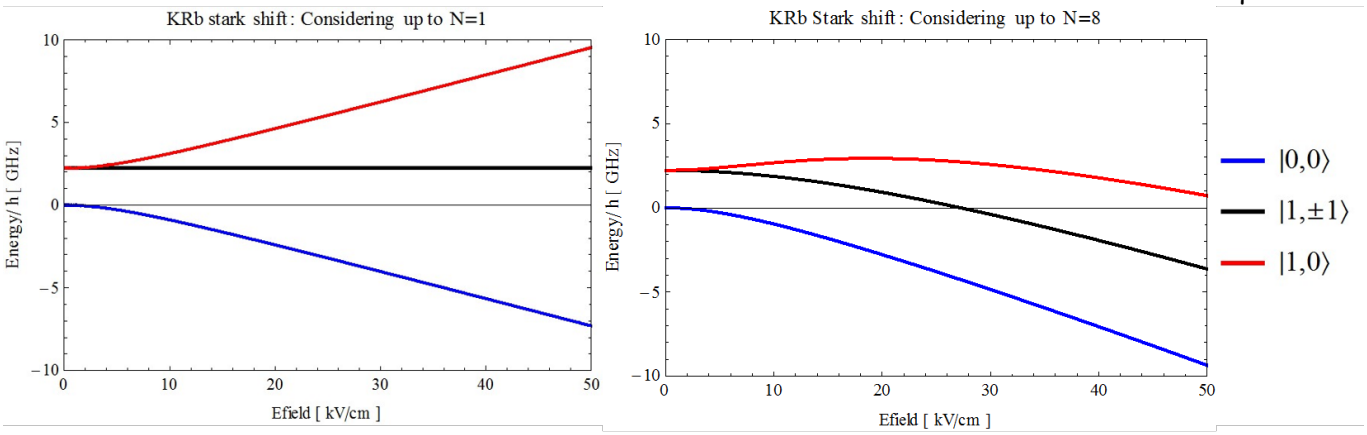

Figure 2.2: The Stark shift on $|0,0\rangle$ and $|1,0\rangle$ states. The states shown are labelled by the states at zero electric field in which they are adiabatically connected to.

2.1.2 Induced Electric Dipole Moments

An induced electric dipole moment is closely related to the Stark effect. Calculating the Stark shift for the rotational energy levels allows us to look at how the electric dipole moment of each state varies with field strength. Writing the Stark shift in terms of the critical electric field allows us to calculate the dipole moment using [10],

$$\mid d_{induced} \mid = \frac{\partial E_{rot}}{\partial \varepsilon} \tag{2.5}$$

where is ε is again the magnitude of the electric field and E_{rot} is the energy for rotational transitions developed through Eqns. 2.3-2.4.

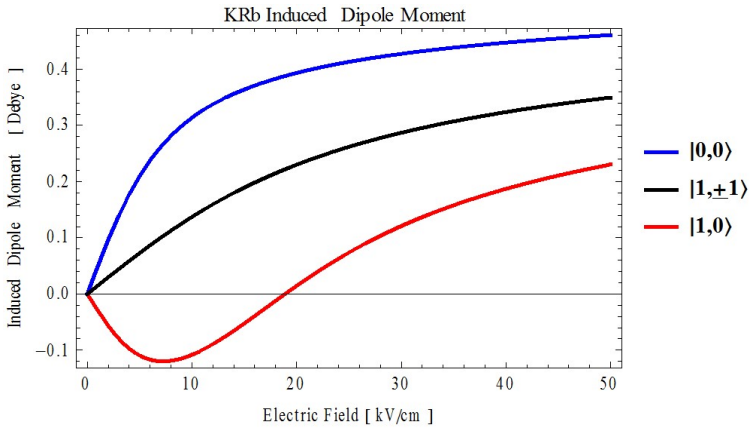

Figure 2.3: Dipole moments of the first two rotational states for KRb. Like with Stark shift in Figure 2.1, the $|1,\pm1\rangle$ states remain degenerate. Again, the states are labelled by where they adiabatically connect at zero electric field.

This shows that the strongest dipole moment of KRb is found in its rotational ground state. Furthermore, notice the size of the dipole moment varies with changing electric field for all states. This highlights the particular significance in applying an external electric field to our molecules. By doing so we gain the ability to tune the dipole moments which presents a means to tune distrength of dipole-dipole interactions can be tuned. This is made clear by the following Hamiltonian, Eqn. 2.6, which describes quantum magnetism between two molecules[2] that can be realized with dipole-dipole interactions of molecules pinned in an optical lattice.

$$\hat{H} = \frac{1}{2}\sum_{i\neq j} \frac{1-3\cos^2\theta_{i,j}}{\mid r_i - r_j \mid^3}\left[\frac{J_\perp}{2}(\hat{S}_i^+\hat{S}_j^- + h.c) + J_z\hat{S}_i^z\hat{S}_j^z\right] \tag{2.6}$$

where the first term describes both the anisotropy[3] of interactions and $J_\perp \equiv 2d_{\uparrow\downarrow}^2$, $J_z \equiv (d_\uparrow - d_\downarrow)^2$, $\hat{S}_i^+$ and $\hat{S}_j^-$ are the usual raising and lowering spin operators, and $\hat{S}_i^z\hat{S}_j^z$ are the

[2] i and j label the two molecules whose spin interaction is described by $\hat{H}$.

[3] Anisotropy arises from stronger a coupling between molecules in the xy-plane and a weaker coupling between molecules along the z-axis.

projections of rotation onto the z-axis. The form of J_z tells us the strongest interactions from the term come from states with greatest difference in dipole moments. Eqn.2.6 is called an XXZ spin model [8], where XX refers to an equal coupling of spins in the xy-plane, and Z refers to a weaker coupling along the z-axis. A unique feature of this model is that with $J_\perp = J_z$ we recover the Heisenberg (XY) model and with $J_z = 0$ we recover the Ising model – two fundamental theories of spin interactions in condensed matter physics. This shows us that external electric fields can be used to tune dipole moments in molecules. These physics are essential for studying spin interactions in the KRb experiment.

Chapter 3

The KRb Machine

3.1 First Generation

Emerging from previously demonstrated levels of control over atomic gases found in JILA came the motivation for creating hetero-nuclear "Feshbach" molecules from ultracold ^{40}K and ^{87}Rb atoms. Due to complexities involved with directly cooling existing molecules, the idea to form loosely bound molecules from previously cooled atomic gases presented a novel new way to circumvent these intrinsic challenges. A desire naturally followed to create and study hetero-nuclear molecules in their absolute (lowest rotational, vibrational, and electronic) ground state. Such an experiment began in 2003 when J. Zirbel and K.-K. Ni began construction of the first generation KRb ultracold molecule apparatus. A few years later the experiment demonstrated success in forming loosely bound "Feshbach molecules" from ^{40}K and ^{87}Rb atoms [11]. From this point, efforts were made by K.-K. Ni and co-workers along with advisors Deborah Jin and Jun Ye to transfer the loosely bound molecules into their lowest ground state, which was ultimately achieved in 2008 [10].

3.1.1 Experimental Limitations

As mentioned previously, one of the most exciting features of dipolar molecules is the ability to control their electric dipole moments with external electric fields. In the absence of an electric field, a ground state polar molecule exhibits essentially no electric dipole moment making dipole-dipole interactions effectively non-existent. With this in mind, a

parallel plate capacitor was implemented on the outside of the experimental science cell in order to tune the molecules' electric dipole moments. However, in short time, several limitations of the design were realized. First, due to the close proximity of the parallel plates to nearby electrical grounds, dielectric breakdown (arcing) set an upper bound on electric field strengths to around $5kV/cm$ limiting dipole moments to $\sim$30% their maximum value. Secondly, a variation in plate spacing of $\sim 25\mu$m/cm resulted in an appreciable cloud shift that was measured to be roughly $20\mu\text{m}/(kV/cm)^2$. With cloud sizes equal to $\sim 100\mu$m in diameter and electric fields strengths ranging from 1-$5kV/cm$, this was a significant effect. Lastly, having the capacitor plates external to the science cell resulted in residual fields from the polarized glass. This proved problematic for determining the constantly shifting resonant frequencies needed for STIRAP (STImulated Raman Adiabatic Process), the process which transfers molecules from a loosely bound state to their ground ro-vibrational state.

In spite of the limitations set by the electric fields in the first generation apparatus, there are many interesting paths that have since been taken that do not require high strength external fields. In fact, the last six years have brought about a number of successes in studying the dynamics and intricacies of ultracold KRb molecules. Over this time the experiment has studied dipolar collisions [12], ultracold chemical reactions [13], long-lived molecules in optical lattices [14], and lattice spin models [15], i.e., XXZ model in Eqn. 2.6. Ultimately the first generation experiment has been a tremendous success, so much so that efforts are currently being made to create a second generation apparatus.

3.2 Second Generation

Looking to the future, the second generation apparatus is nearing completion. It is designed to meet many of the experimental limitations realized in the first generation. Figure 3.1 shows the second generation experiment nearly prepared to replace the first generation.

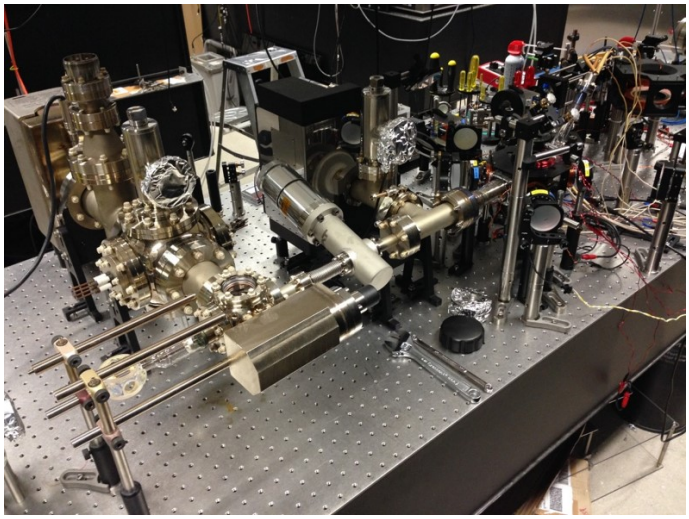

Figure 3.1: Generation II KRb apparatus.

3.2.1 New Features for Electric Fields

The second incarnation of the KRb experiment provides many new possibilities for studying molecules. Expanding on the capacitor plate design of the previous generation, the new system offers two Indium Tin Oxide (ITO) coated capacitor plates in addition to four tungsten metal-rod electrodes all contained within vacuum. This provides a promising solution for the residual fields and arcing seen in the previous experiment. When combined, electrodes and capacitor plates provide the ability to generate uniform fields as well as field gradients. Although the purpose of the capacitor plates is to generate precise DC fields– described with detail in Chapter 4 – the four tungsten rods are capable of creating DC fields as well as be driven at AC frequencies in order to produce microwaves to drive rotational transitions in the molecules. Unlike in the old apparatus, the new plates are in vacuum and spaced 6mm apart allowing them to handle ∼22kV/cm before voltage breakdown. In addition, the four metal-rod electrodes can create field gradients as large as $10\text{kV}/cm^2$. Figure 3.2 shows the new science cell with the six electrodes for electric fields.

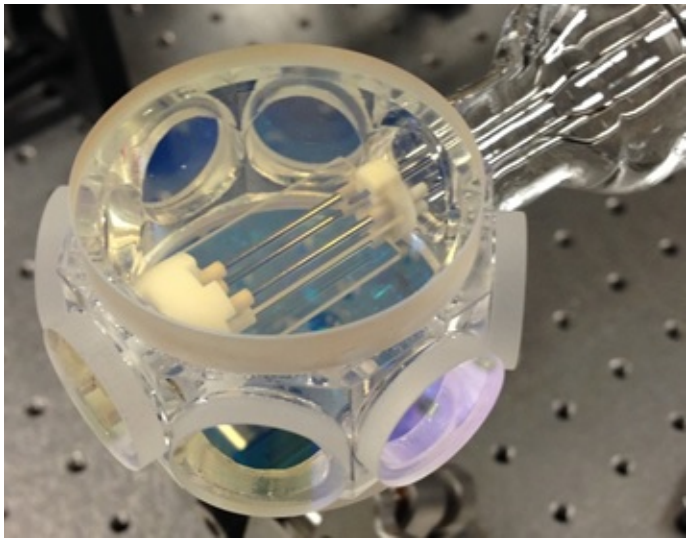

Figure 3.2: Science cell of the generation II KRb experiment. Enclosed are two ITO-coated capacitor plates for generating uniform electric fields and four tungsten metal-rod electrodes capable of generating electric gradients.

Given the allowances provided by this design, there are three primary functions the electric fields will serve for future experiments: evaporatively cooling polar molecules, selectively imagining lattice sites, and providing a means to precisely tune dipole-dipole interactions. The necessary stability of the electric field varies among these three functions with critical stability levels required only for transferring between rotational states in the presence of an electric field. The following chapter will address the requirements on stability for driving these rotational transitions, while the immediate subsequent sections provide a general description of the functions the electric fields will serve.

3.3 Applications for electric fields

3.3.1 Evaporative Cooling

Evaporative cooling is a common technique in ultracold atomic physics used to reduce the translational motion of atoms in order to reach quantum degeneracy [16] where low temperatures and high densities are seen. The technique exploits the familiar and everyday

phenomenon of evaporation. This occurs when atoms/molecules have enough energy to escape a potential barrier in which they are confined. A common analogy is steam rising from a cup of hot coffee where the steam is a result of molecules possessing the necessary energy to leave the surface of the liquid. While readily used for cooling atoms to sub-micro Kelvin temperatures, the technique has been difficult to demonstrate for cooling molecules. Having this ability could be important for bringing pre-existing molecules into the quantum regime, expanding the opportunities for researching ultracold interactions. The ability to generate electric field gradients in the new KRb apparatus provides a potential means for evaporatively cooling polar molecules. In Figure 3.3, a simple illustration of the proposed technique is shown.

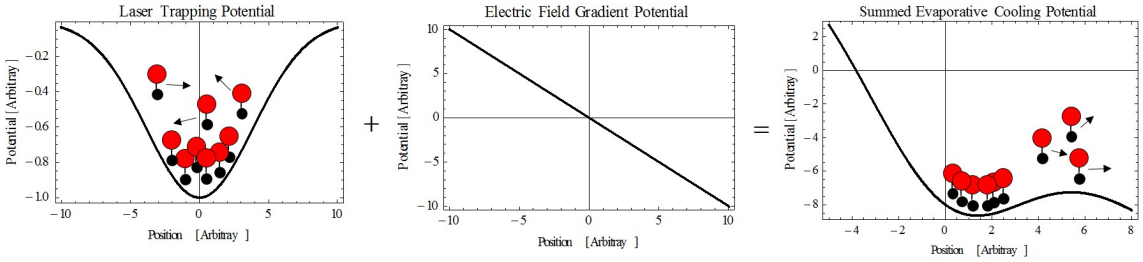

Figure 3.3: A scheme for evaporatively cooling polar molecules in a 2D geometry. Starting with previously formed molecules subjected to a one dimensional optical lattice, applying an electric field gradient tilts the trapping potential allowing more energetic molecules to escape, resulting in only the coolest molecules remaining.

3.3.2 Selective Imaging

In addition to new possibilities for evaporatively cooling polar molecules, electric field gradients provide a new tool for selecting lattice sites to be imaged. Imaging molecules in our experiment is done by a process of absorption imaging, where one images the shadow of the atom or molecule cloud cast by a beam of light on resonance with an atomic or molecular transition. Providing an electric field gradient across a cloud of molecules allows one to

exploit the Stark effect to tune their resonant energies. Therefore, varying an electric field gradient provides a method for selecting the location of molecules that are imaged. This could present the ability for single-site resolution of molecule formation which could prove useful for diagnosing the preparation of our molecules. Figure 3.4 shows the idea behind this process.

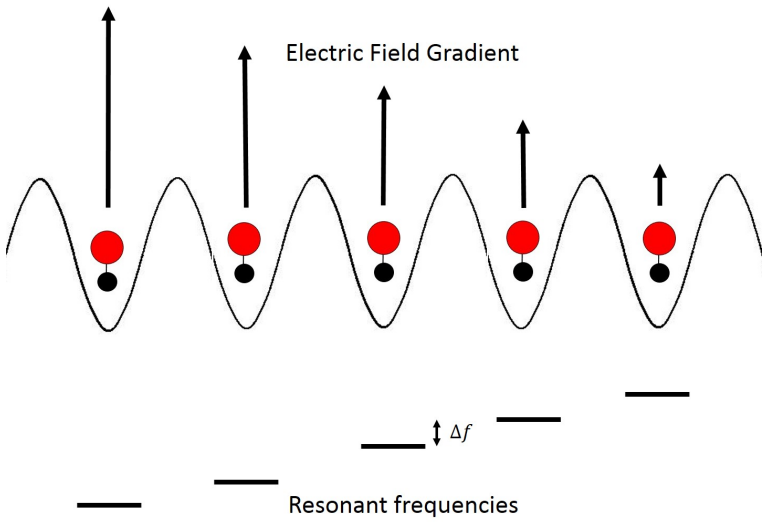

Figure 3.4: Applying an electric field gradient across a lattice of molecules can shift their resonant frequencies in order to selectively imaging individual sites.

3.3.3 Tunable Interactions: Ramsey Spectroscopy and Spin Transport

One of the most exciting tools presented by external electric fields is the ability to precisely tune dipole-dipole interactions in an ordered lattice structure. These types of interactions explicitly depend on the strength of electric dipole moments between molecules which can be precisely tuned with high strength electric fields. As a result, having control over dipole-dipole interactions in addition to lattice geometries provides a new and novel method for simulating the dynamics quantum magnetism [8].

The basic idea for simulating quantum magnetism with molecules is creating a system in which a molecular degree of freedom common among a large number of molecules is coupled

by dipole-dipole interactions. Given this, we would like to use the rotational energy levels to create a two state system in order to study this phenomenon. There are two types of experiments we will consider for purposes of determining requirements for electric stability. These are Ramsey spectroscopy and Spin transport.

A Ramsey spectroscopy experiment is one in which a quantum system is prepared in a single spin state and allowed to evolve in time, without external influences. After some time, t, the system is measured to analyze variations in spin (rotation). In our experiment, we create an equal superposition between two states defined to be $|\uparrow\rangle$ and $|\downarrow\rangle$ by applying a $\pi/2$ pulse from a microwave source. This sort of experiment requires transfer efficiency to be high in order to resolve any changes that have occurred. In the presence of an electric field, this experiment will require field uniformity and stability in order for transfer fidelity to be near that of previous experiments, $>99\%$.

The second experiment makes use of electric field gradients to prepare a system for studying transportation of spin across a lattice. This is referred to as a "Spin Transport" experiment. Using an electric field gradient to shift the resonant energies between neighboring lattice sites, as in Figure 3.4, it may be possible to excite individual molecules in a 1D lattice, single rows in a 2D lattice, or single layers (pancakes) in a 3D lattice, and observe how spins propagate over time. This may present a novel method for studying spin-orbiting coupling using polar molecules [17]. The key to this type of experiment is ensuring the electric field gradient is stable enough to drive transitions in molecules at only spatially desired site(s). In this case, since it is an incoherent process, transfer fidelity need not be $>99\%$, instead a fidelity of $\sim 90\%$ would be sufficient.

Chapter 4

Experimental Requirements for Electric Field Stability

One of the most sensitive elements in our experiment is the transition frequency needed to drive rotational transitions with microwaves. With the microwave source fixed, changes in the transition frequency correspond to changes in the probability of driving a transition. As a result of the Stark effect, shown in Figure 2.2, this transition frequency will shift with fluctuations in electric field. Therefore, ensuring a high transition fidelity requires the electric field be sufficiently stable over various timescales.

4.1 Time Scales for Electric Field Stability

If the frequency needed to drive a rotational transition drifts over the course of the several hours needed to take data, the efficiency of driving rotational transitions may also drift, which would be detrimental to the experiment. Given this, drifts in the value of the electric field over these time frames will be extremely important in future experiments for ensuring repeatability. In addition to long timescales in which the experiment will require repeatability for large sets of data, the electric field must also be stable over the time frame of individual experimental runs. In general, the process for running an experiment with electric fields will involve creating molecules at zero field and ramping in 1ms to a desired field strength to perform an experiment. Following this, the field will be ramped down 1ms in order take a measurement. Figure 4.1 shows depicts this process.

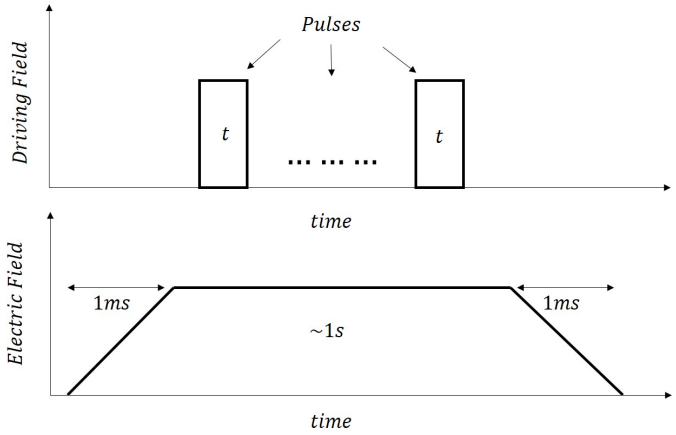

Figure 4.1: During an individual experiment an electric field will be ramped up to a desired value between 1-22kV/cm, held for ∼1s and ramped down to image. During high field, a series of pulses will change molecular states as required by the particular experiment.

After the field is ramped to a desired value, a microwave pulse will drive molecules into an excited state. This requires fields to be stable over the time in which the microwave field is on. Past experiments have required complex pulse sequences. In the new experiment this will extend the times necessary for electric field stability to beyond individual pulses. Ultimately, the electric stability over short times scales determines the experiments that can be performed, while long term stability determines how repeatable an experiment is. With this in mind, we can consider the stability needed to perform the two experiments proposed in the previous chapter, Ramsey spectroscopy and spin transport.

4.2 Rabi Frequencies for Driving Transitions

Both of these experiments have requirements on the probability of driving molecules into an excited state. This probability is inherently dependent on the stability of the electric field. We can begin by considering the probability that a molecule is promoted into its excited state. For a two-level system, the probability of driving a transition can be determined by looking at the Rabi oscillations in the frequency domain [18]. In the presence of a driving

field, the probability of finding a molecule in its rotationally excited state is given by,

$$P_{|1,0\rangle} = \frac{\Omega_R^2}{\Omega^2} \sin^2\left(\frac{\Omega t}{2}\right) \tag{4.1}$$

where Ω is the generalized Rabi frequency given by $\Omega = \sqrt{\Omega_R^2 + \delta^2}$, Ω_R is the Rabi frequency which is proportional to the driving field strength (microwaves for rotational states), and δ is how far the field is away from resonance, known as detuning. Eqn. 4.1 shows that transition probability decreases with increasing detuning from resonance. In this case, as a result of the Stark shift, detuning will occur if there are any fluctuations in the electric field. The rate at which the transfer fidelity drops off for off-resonant driving fields decreases for increasing Ω_R. Thus, in principle, increasing the Rabi frequency minimizes sensitivity to fluctuations in the electric field. However, if the Rabi frequency is too large, it is possible to excite molecules to nearby states that have a similar resonant frequency. Therefore, it is necessary to find an appropriate Rabi frequency that results in the desired transition fidelity while exciting only the states of interest. This can be understood by plotting the transition probability for various Rabi frequencies.

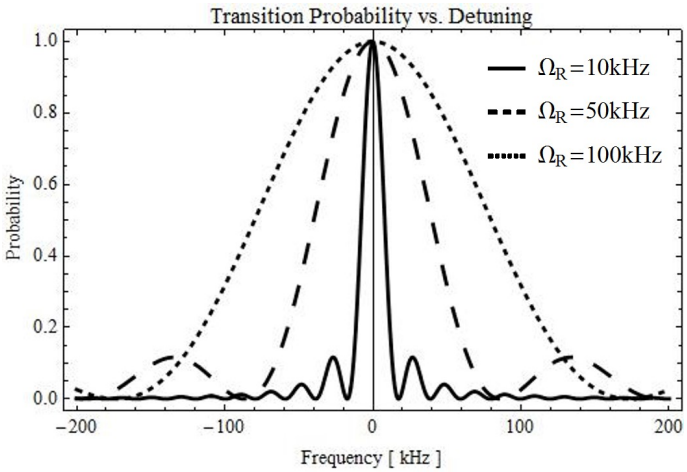

Figure 4.2: Probability of transition from $|0,0\rangle$ to $|1,0\rangle$ for three different Rabi frequencies.

Varying the Rabi frequency scales probability width. Therefore, if we know the detuning from resonance of a neighboring state we can determine the Rabi frequency necessary to ensure the neighboring states has a low chance of being excited. In order to ensure this we can force the inequality,

$$\frac{\Omega_R^2}{\Omega_R^2 + \delta^2} \leq 0.01 \tag{4.2}$$

which informs us that $\Omega_R \leq \delta/10$. Given this, the distance to the nearest neighboring state (for both experiments) tells us the necessary Rabi frequency, which in turn allows to calculate the probability of transition for the desired state. For both experiments, we need to ensure a specific hyperfine state is excited. Without a calculation for the separation in hyperfine states, I used a plot found in our lab to make an approximation.

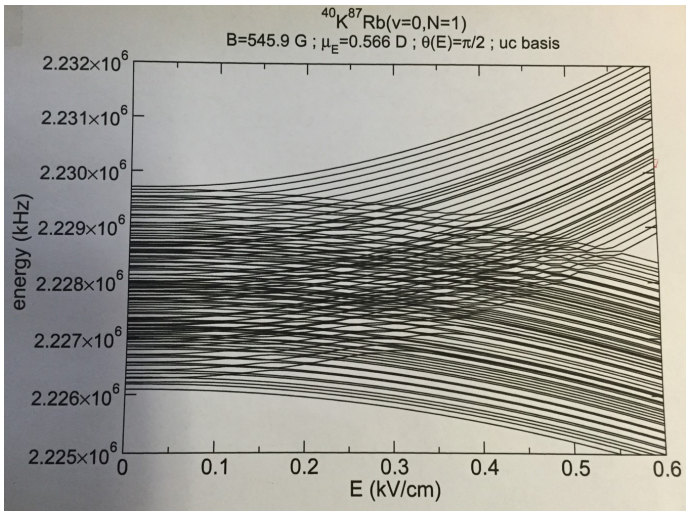

Figure 4.3: Hyperfine structure of KRb in its N=1 rotational state. Figure made by Goulven Quemener and John Bohn.

Assuming that after 550kV/cm the separation between states remains relatively fixed, we can estimate the separation to be ∼100kHz. With this, Ω_R=10kHz for the Ramsey spectroscopy

experiment. For the Spin transport experiment, the Rabi frequency is again determined by finding frequency separation between nearest neighboring states. However, for this experiment, the separation in frequency between adjacent lattice sites depends on electric field strength. We must look at the molecules' sensitivity to fluctuations in electric field in order to determine if the separation between lattice sites compares to the separation between hyperfine states.

4.3 Sensitivity and Transition Probability

Referring back to the Stark shift for KRb, the sensitivity to fluctuations in the electric field can be found by looking at how the transition frequency between $|0,0\rangle$ and $|1,0\rangle$ changes with changing fields. Figure 4.4 shows the result of calculating $\partial\Delta E_{rot}/\partial\varepsilon$, where E_{rot} is in frequency units (f=E/h) in order to relate to detuning.

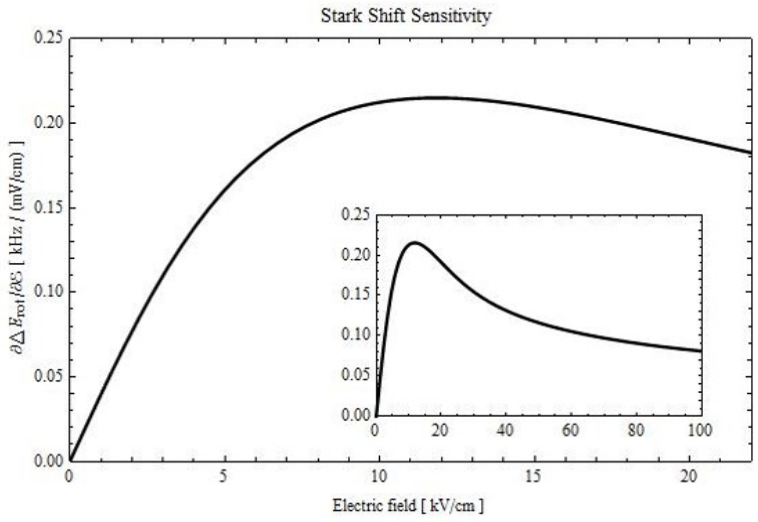

Figure 4.4: Sensitivity to variations in electric field strength, $\partial\Delta E_{rot}/\partial\varepsilon$. The inset on this plot shows the molecule's sensitivity up to 100kV/cm. This shows that the most sensitive field strength is near 12k/cm.

This plot shows that the molecules are most sensitive to instability in the electric field around

12kV/cm. It also provides a method for determining the separation between states of adjacent lattice sites from which we can then determine the necessary Rabi frequency for the spin transport experiment. The optical lattice used in our experiment is 1064nm, providing for roughly 1μm lattice spacing. Using the maximum electric field gradient of the new apparatus, 10kV/cm^2, we can can plot the frequency shift between two lattice sites against the electric field felt at a single site. shown in Figure 4.5.

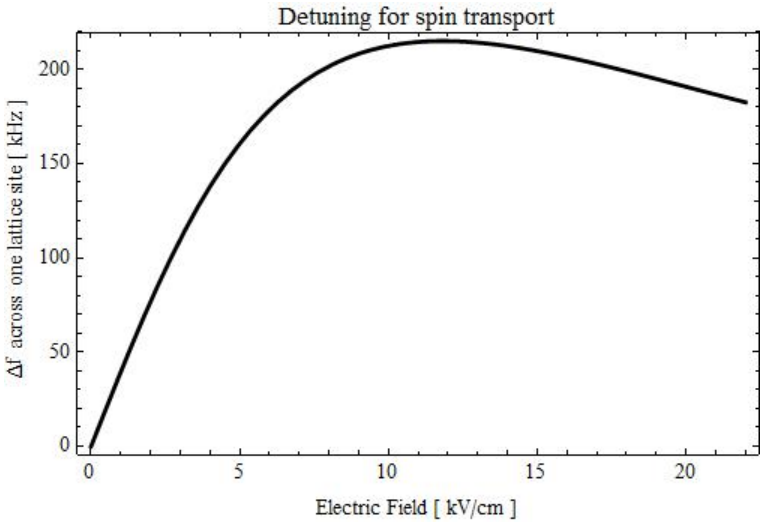

Figure 4.5: Frequency separation between neighboring lattice sites, in a 1064nm lattice. The x-axis represents the electric field applied to a single lattice site. Neighboring sites along the direction of the field gradient feel a Stark shift which lends to a separation in their resonant transition frequencies.

With the Rabi frequency being $\delta/10$ we find at fields $\leq$3kV/cm, the shift between neighboring states is greater than the shift due to hyperfine splitting. Therefore beyond $\sim$3kV/cm, we will use Ω_R=10kHz and below we will use the Rabi frequency determined by neighboring lattice sites.

For the remaining chapters, we will use the dimensionless quantity of Parts Per Million (ppm) for characterizing the fractional electric field stability for an average field strength. It

is defined by 1ppm = $(\Delta V_{pk-pk}/V_{avg}) \times 10^6$. For example, 1ppm of an electric field strength of 1kV/cm is 1mV/cm. Fluctuations in the electric field result in detuning from resonance which allows us to plot the transition probability, given by Eqn 4.1, as a function of this new quantity. Writing detuning as a function of fractional stability (ppm) we have,

$$\delta = \frac{1}{2}\left(\frac{\partial \Delta E_{rot}}{\partial \varepsilon}\right)\varepsilon \times 10^{-6} \tag{4.3}$$

With this expression we may plot the transition probability, $P_{|1,0\rangle}$, for different electric field strengths, shown in Figure 4.6.

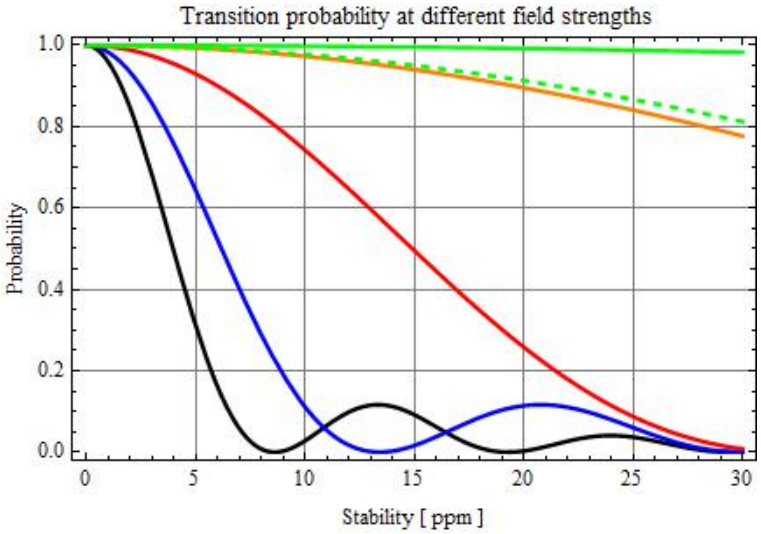

Figure 4.6: Plot shows $P_{|1,0\rangle}$ vs fractional electric field stability for 5 different average electric field strengths with $\Omega_R = 10kHz$, 22kV/cm in black, 12kV/cm in blue, 6kV/cm in red, 3kV/cm in orange, and 1.5kV/cm in solid green. Above 3kV/cm both Ramsey spectroscopy and spin transport use $\Omega_R = 10kHz$, however, below 3kV/cm, spin transport requires a different value of Ω_R. Dashed green shows the transition probability for spin transport at 1.5kV/cm and $\Omega_R \sim 6kHz$.

This gives an idea how significant the choice of electric field is for driving a transition with high efficiency. At all fields above 3kV/cm, spin transport is less sensitive to instability than Ramsey spectroscopy because it requires lower transfer fidelity. Below 3kV/cm how-

ever, spin transport becomes more sensitive because the frequency shift between neighboring lattice sites is less than that of hyperfine splitting. This requires a particular Rabi frequency for spin transport at each electric field strength <3kV/cm. In table 4.1 I have listed the fractional stability necessary for each experiment at the field strengths plotted above.

Electric Field	22kV/cm	12kV/cm	6kV/cm	3kV/cm	1.5kV/cm
Ramsey Spectroscopy: $P_{\|1,0\rangle}$≥99%	0.5ppm	0.8ppm	1.8ppm	6ppm	22ppm
Spin Transport: $P_{\|1,0\rangle}$≥90%	1.25ppm	2.5ppm	6ppm	19ppm	21ppm

Table 4.1: Experimental requirements on stability for given electric field strengths.

Table 4.1 shows a range of stability requirements for given field strengths. In order to run any type of experiment at fields providing strong dipole-dipole interactions, ε ≥1.5kV/cm, the electric field must be stable to better than $\sim 22kV/cm$. The dipole-dipole interactions to be studied in both experiments strongly depend on the electric field strength. Due to this we would like the field stability to be better than 22kV/cm in order to provide a large of range of tunable interactions. This level of stability should be achievable at high voltage, while stability levels near ≤1ppm is likely impossible. Given this, we determined that a conservative goal would ≤10ppm, while a slightly more advantageous goal would be ≤5ppm.

Chapter 5

Designing a Precision, Programmable, High-Voltage Source

5.1 The System

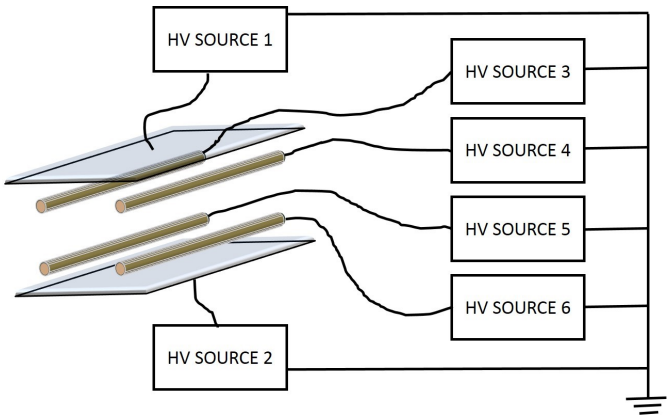

Figure 5.1: Setup for generating arbitrary electric fields in the second generation experiment. There is one high-voltage source for each electrode/capacitor plate, all referenced to ground, allowing each to be controlled independently.

In its most basic form, Figure 5.1 depicts the layout for generating high strength electric fields in the new science cell. Referencing each high-voltage source to ground enables all six sources to be varied independently from one another. The setup for each high-voltage source is shown below in Figure 5.2. Common to all sources is a Field Programmable Gate Array ($FPGA$) that enables precisely timed commands to be written to the six Digital to Analog Converters (DACs) from a single computer.

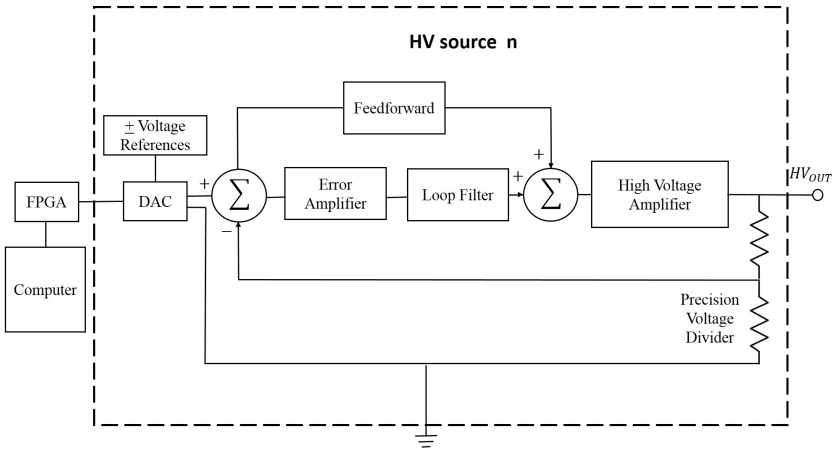

Figure 5.2: Block diagram representing each of the six high-voltage sources.

Each source has its own low-voltage *DAC* that is referenced off two stable zener diodes (± *Voltage References*). The DAC signal is amplified by a high-voltage amplifier (gain of 1000) and controlled using negative feedback through a *precision voltage divider*. This constitutes a control loop, which will be discussed in detail in 5.1.4. Using the *Error Amplifier* stage, any discrepancy between the high-voltage signal and requested DAC signal is amplified in order to better suppress error. The amplified error signal is fed into a carefully designed *Loop Filter* that attempts to fix the amplified discrepancy, forcing the high-voltage output to exactly mirror the low-voltage DAC input. Ultimately, the high voltage signal (HV_{out}) is fed to one of the six electrodes within the science cell. The high-voltage source also provides the option to use *feedforward* in which the DAC signal is allowed to bypass the error amplifier and loop filter in order to reduce the burden being placed on the feedback loop. The following sections discuss the key elements to this design, namely, the *Voltage References*, *DAC*s, *High-Voltage Amplifier*, and *High-Voltage Control Loop*. Note the data shown in the following sections was taken for one circuit setup. The final version will have six of the proposed design discussed below.

5.1.1 Voltage Reference

The achievable stability using this high-voltage system is predicated upon the stability of the ±voltage references provided to the DACs. Ultimately, the stability of the DACs set the stability the control loop will attempt to match. Due to this, a considerable amount of time was spent determining an appropriate design for the references so as to provide as clean a signal as possible over both short and long time scales. As a starting point, we chose to use a precision temperature stabilized zener diode, called the LM399. This reference outputs 7V, perfectly matching the limit set on the electric fields after x1000 amplification (22kV/cm × 0.6cm = 14kV = ±7kV). This reference is heralded for its 0.3 ppm/°C temperature coefficient and low 7μV RMS noise (over a 10Hz-10kHz range). While better references do exist, such as the LTZ1000, the LM399 requires a simple circuit layout, is relatively inexpensive, and met the performance characteristics desired.

There were numerous factors considered when laying out the design for these ± voltage references. To our surprise, it was quite difficult to achieve the performance specified by the datasheet. Achieving stability on this level requires careful consideration of the various limiting effects such as thermocouples and the parasitic issues with RLC components. Trouble shooting these issues involved using a Digital Multimeter (DMM) and a Fast Fourier Transform (FFT) spectrum analyzer. In order to reduce the output noise of the LM399 zener diodes (found in Figure A.1), we used a RC low-pass filter with 0.1Hz corner frequency. The low-pass filter required an ultralow noise op-amp ($0.1\mu V_{pk-pk}$), as a voltage follower, to ensure that the reference circuit can drive all six DACs. The most interesting elements used for the reference are zero Ohm resistors. The resistors were placed in the voltage return lines in order to thermally match solder points in the voltage path. This was found to have a significant effect on the long term stability of the reference circuits, and consequently the DACs. The final design of the reference circuit can be found in Figure A.7.

To determine the output noise of the reference circuits, we used the SR780 FFT machine

from the JILA electronics shop. Figure 5.4 shows the AC noise spectrum measured in Power Spectral Density (PSD) units from 2Hz to 102kHz.

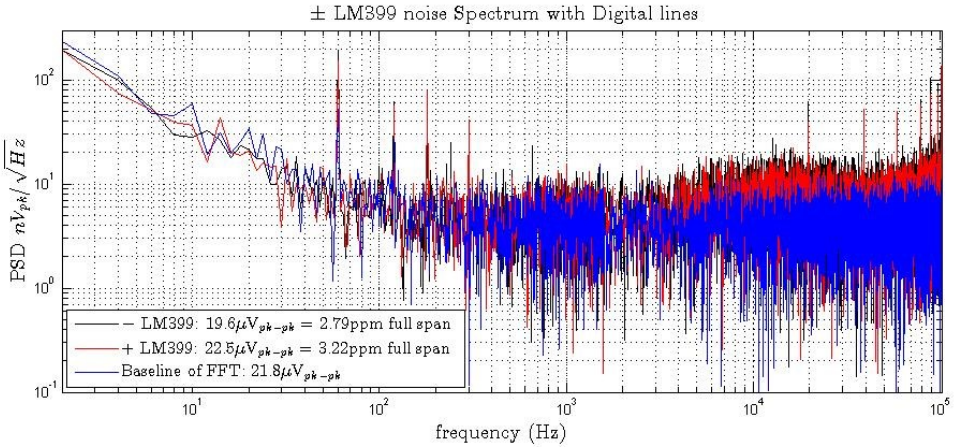

Figure 5.3: Noise spectrum of both ±voltage references, red and black respectively, and the measurement noise floor of the SR780 FFT spectrum analyzer in blue. Increase in noise at higher frequencies is believed to be a result of the ±12V regulators used prior to the references, see Figure A.4. Noise at 60Hz and its associated harmonics we believe is a result of noise pick up within the KRb lab, see Figure A.5. Noise calculations for ppm found in the plot legend were calculated using discreet integration of the spectrum according to the trapezoidal rule from 2Hz-102kHz.

The output noise of both LM399 reference circuits are well below that specified by their datasheet (Figure A.1), showing our design was effective. The ppm values indicated on the plot were found by numerically integrating the spectrum according to the trapezoidal rule[3] . The noise across the frequency range shown is close to the minimum value the FFT can measure (the baseline). However, there is additional noise at 60Hz and its harmonics as well as at higher frequencies. We believe there are two sources for this noise: the 12V regulators prior to the reference (spectrum in Figure A.4), and noise within the lab being rectified onto the circuit (spectrum in Figure A.5). This data was taken with filters on all inputs and

[3] Trapezoidal rule: $\sum \frac{V(i)+V(i+1)}{2}\Delta f$

outputs of the box containing the LM399s and DAC. Filter designs can be found in Figure A.6.

In order to determine the short term repeatability of running these experiments, we used an Agilent 34410A Digital Multimeter (DMM) to measure DC stability. We determined the sampling rate at which the DMM could resolve voltage changes of $\leq$1ppm to be 30Hz. Figure 5.4 shows the short term stability ($\sim$30 seconds) of the positive LM399 reference circuit. The negative reference performs at very comparable levels.

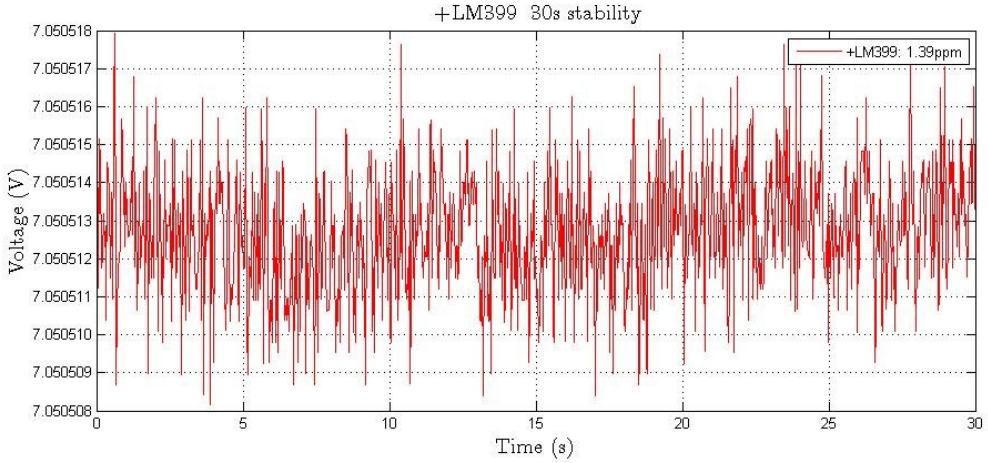

Figure 5.4: Short term +LM399 drift measured with Agilent 34411a digital multimeter. Data taken at 30Hz sampling rate on the 10V range for 1000 data points ($\sim$30s). Data corresponds to $V_{pk-pk} = 9.73\mu$V, where the noise floor of the device is $\sim 8\mu$V.

Since the reference voltage is fixed, its long term stability is extremely important for the overall repeatability of the DAC and high-voltage. We found that power cycling the reference circuits as well as changing its resistive load resulted in small changes in reference voltage. Shown below in Figure 5.5 is data for the voltage drift of the -LM399 reference circuit over the course of 30 days. The data before day 13 shows the effects of power cycling the reference as well as connecting and disconnecting measurements leads. After day 13 the reference remained powered and connected to the digital multimeter.

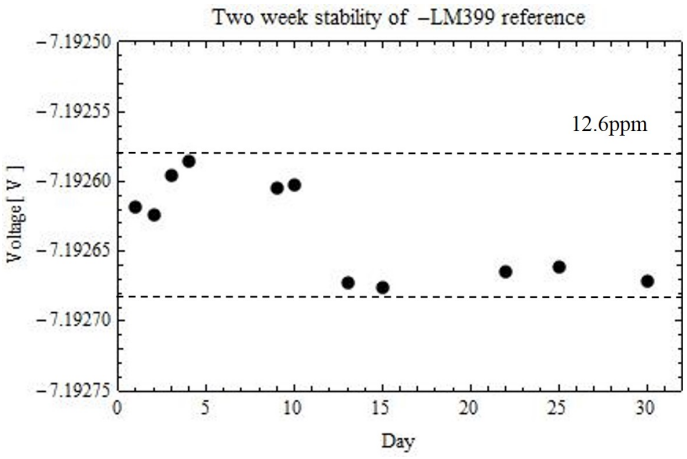

Figure 5.5: Month long drift of -LM399 reference using Agilent 34411a digital multimeter. Each data point is an average over 500 data points at 30Hz sampling rate.

5.1.2 Digital to Analog Converter (DAC)

The ±voltage references set the ±standards for the DACs. The DAC chosen for our design (AD5791) has a 0.05ppm/°C temperature coefficient and a 1ppm resolution which allows it to be ramped to maximum voltage with a repeatability of 1ppm. The DAC is programmed using a sequence of pulses show below in Figure 5.6. The bottom signal is the SYNC, which primes the DAC for receiving the code, the middle is the CLOCK which acts as a timing reference, and the top signal provides a pulse train with the code corresponding to the desired output voltage. The ± voltage references are divided using a series of mechanical switches that change the division factor of an internal voltage divider within the DAC.

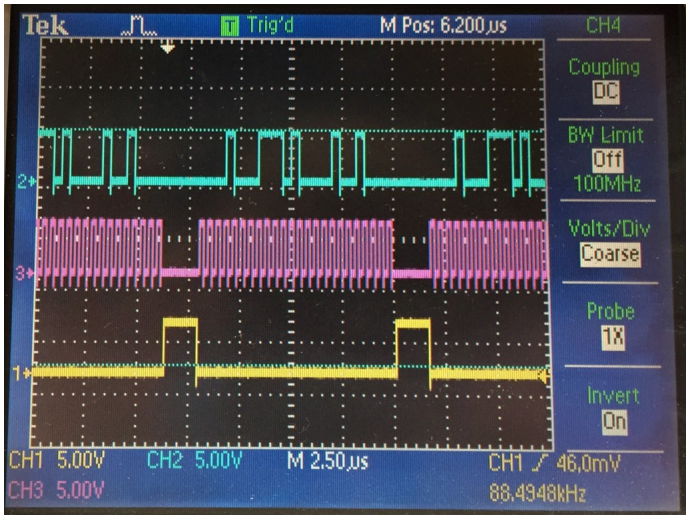

Figure 5.6: Digital pulse sequence of three signals used program voltages to the DAC. From top to bottom the figure shows the, DIGITAL, CLOCK, and SYNC signal. The DIGTIAL signal is the code interpreted by the DAC according to the location of digital high values with respect to the CLOCK. The SYNC is used to prime the DAC for receiving the DIGITAL and CLOCK signals.

Like the ±voltage reference circuit, the DAC required specific attention to achieve satisfactory performance. By design, the DAC has five different grounding locations: one for each voltage reference, one for the digital input signals, one for the analog power, and one for the digital power. We found that all grounds were necessary to see minimum noise levels, however, in order to keep any noise on the digital ground from entering the DAC output path, we found it necessary to insert a 1Ω resistor in series with the analog ground. This makes any ground noise preferentially exit the DAC through the digital ground. The resulting noise spectrum is shown below in Figure 5.7.

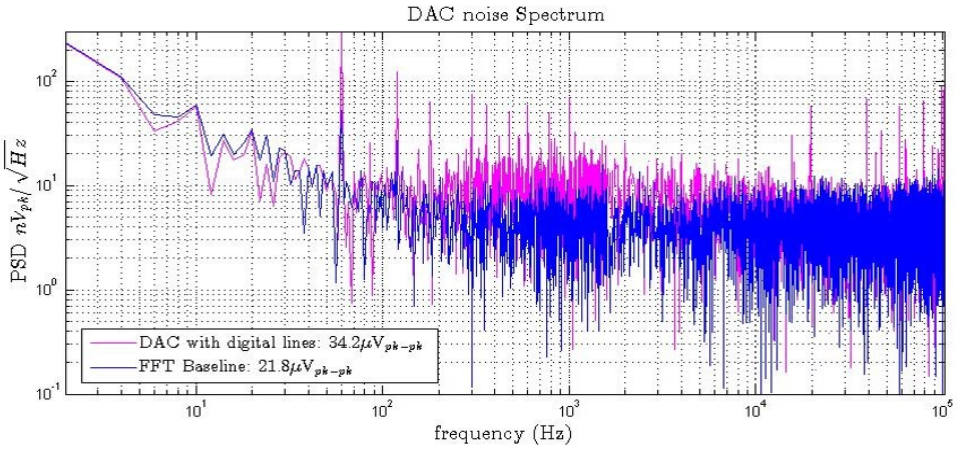

Figure 5.7: Noise spectrum of DAC programmed to +1V. V_{pk-pk} calculated again using the trapezoidal rule from 2Hz-102kHz.

This data in Figure 5.7 was taken at the maximum +7V that the DAC can output based on the LM399 reference. Over the 2Hz-102kHz spectrum measured, the DAC has noise corresponding to ∼4.9ppm. We found changing the DAC output voltage did not significantly change the output noise. As a result, I deemed it more appropriate to list the noise of the DAC in terms of μV_{pk} units.

Figure 5.8 shows the measured short term (∼30 seconds) stability of the DAC programmed to output 0.8V. This voltage was chosen in order to directly compare to the stability of the high-voltage amplifier at 800V, which the DMM is capable of measuring.

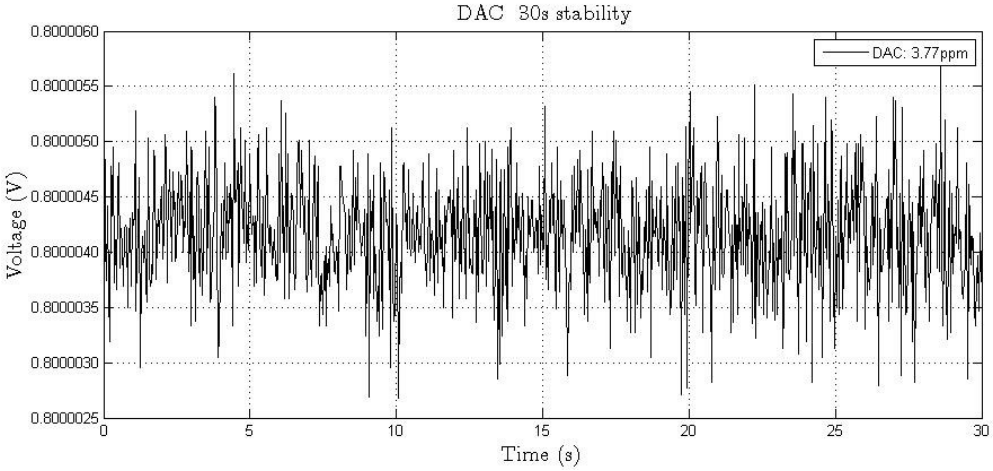

Figure 5.8: Short term DAC drift measured with Agilent 34411a digital multimeter. Data taken with same setup as +LM399 short term drift in Figure 5.4 (30Hz sampling rate for 1000 data points).

The stability was concerning at first as the reference circuit appeared to perform considerably better. We therefore decided to investigate stability of the DAC at different output voltages. The measurement was broken into two voltage ranges, 10V and 1V, in order to gain the best resolution from the DMM. Unlike the AC noise of the DAC, the short term DC stability of the DAC depends heavily on the choice of output voltage, shown in Figure 5.9. This appears to be a fundamental limitation of the DAC. As a way to demonstrate that this was not an artifact of the measurement device, we repeated the measurement using the high-voltage amplifier, which will be discussed in the following section.

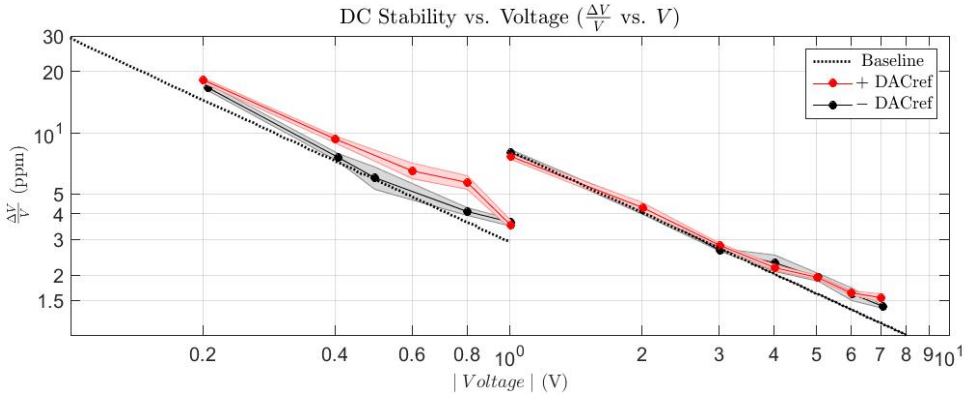

Figure 5.9: Plotted above is the DAC fractional stability, measured in ppm, for different programmed output voltages. Each data point is an average over five 30s trials at 30Hz sampling rate. The shaded error bars are given by the standard error ($\sigma/\sqrt{N}$, where N=5). The Baseline, or instrument noise floor, was found with one 30s run with a 50Ω capacitor at its input and corresponds to $\sim 8\mu V_{pk-pk}$.

We also measured the DAC over the course of the day to determine its long term stability, shown in Figure 5.10. For this measurement we used a sampling rate of 0.6Hz which provides for 0.03ppm resolution at each voltage range. While every long term measurement varies slightly from one another, this is a good representation of the typical performance observed from the DAC over 12 hour measurement periods.

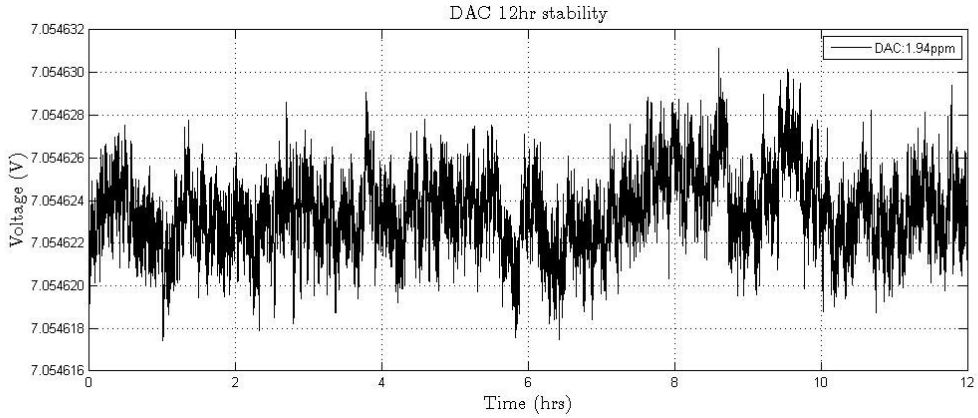

Figure 5.10: Long term drift of DAC programmed to 0.8V. Data taken using agilent 34411a digital multimeter with 12500 data points taken at 2mHz sampling rate.

5.1.3 High-Voltage Amplifier

The high voltage amplifier chosen for our design is a stable high-speed and high-voltage amplifier capable of precise control of output voltages. It can output as much as ±10kV DC or peak AC, which enables electrodes and capacitor plates in the science cell to reach full field strength. The amplifier has a high-voltage bandwidth well beyond the >1kHz bandwidth necessary in order to ramp the electric fields in a 1ms time frame (Bandwidth found in appendix, Figure A.5). It also can be turned on and off by a TTL (digital) signal which allows the amplifier to be placed well out of reach for safety reasons. Since the FFT spectrum analyzer is not capable of measuring high voltage, output noise of the high-voltage amplifier was measured by shorting its input (using a 50Ω plug for impedance matching). Below is the noise spectrum we measured.

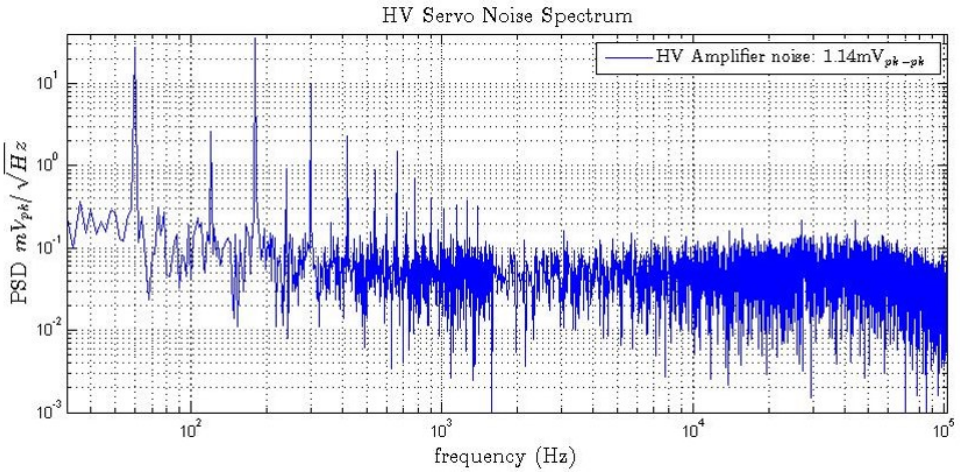

Figure 5.11: Noise spectrum of high-voltage amplifier shorted using 50Ω plug.

While this measurement does not represent the situation that will be seen during normal operating conditions, i.e, high voltage, it provides a minimum noise level to expect from the amplifier.

As mentioned previously, in order to directly compare the long term stability of the high-voltage amplifier to that of the DAC, we amplified the DAC voltage programmed at

0.8V, to 800V. Our DMM is capable of measuring voltages up to 1kV which enabled us to take the following data.

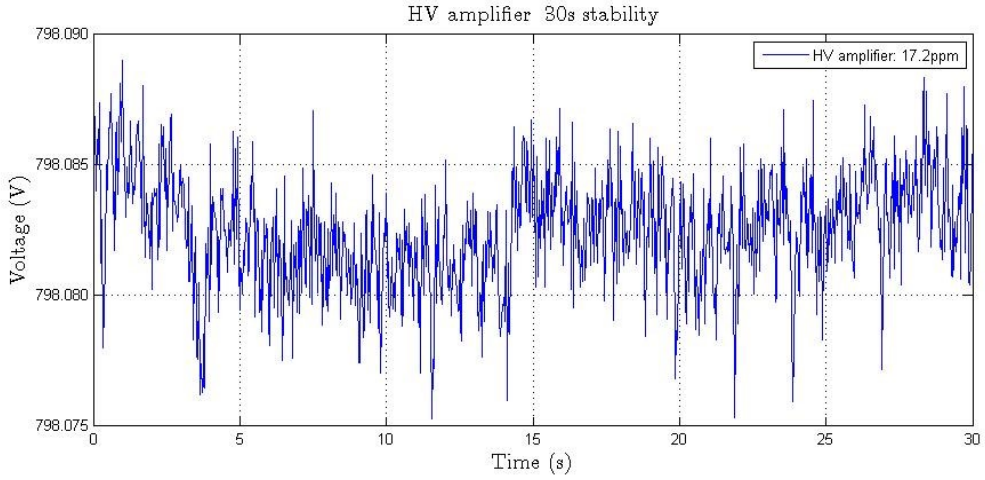

Figure 5.12: Short term amplified DAC drift measured using Agilent 34411a digital multimeter.

By comparison, the high-voltage amplifier is considerably less stable over long periods of time relative to the experiment. Such instability could make the desired value of the ramped voltage fluctuate over the course of experimental runs. We also measured stability for the high-voltage amplifier over longer time periods, as shown in Figure 5.13 below.

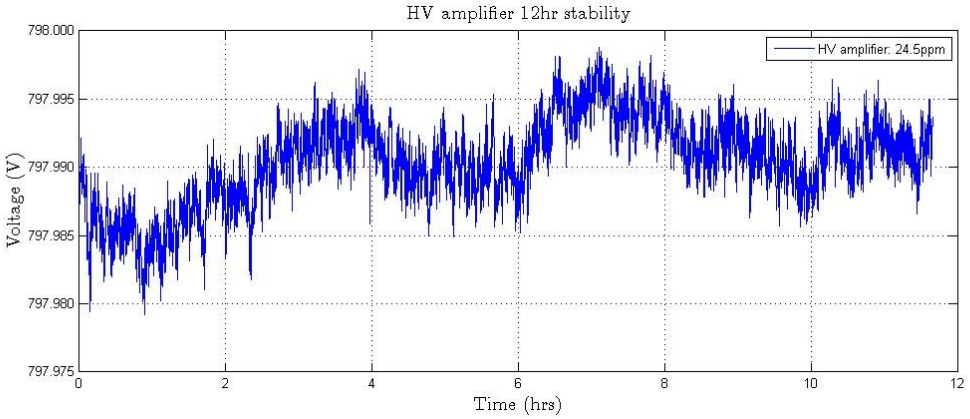

Figure 5.13: Long term drift of high-voltage amplifier with DAC signal input. Data taken with Agilent 34411a digital multimeter using 2mHz sampling for 12500 data points.

Fluctuations in output voltage came as no surprise given the drifts at shorter timescales. Following this, we looked at the high-voltage (amplified DAC signal) stability as a function of output voltage. Figure 5.14 shows the same trend seen with DAC is again seen when using the amplifier. This seems to verify DAC stability depends on output voltage, and as a result, the high-voltage is similarly dependent on the output voltage chosen.

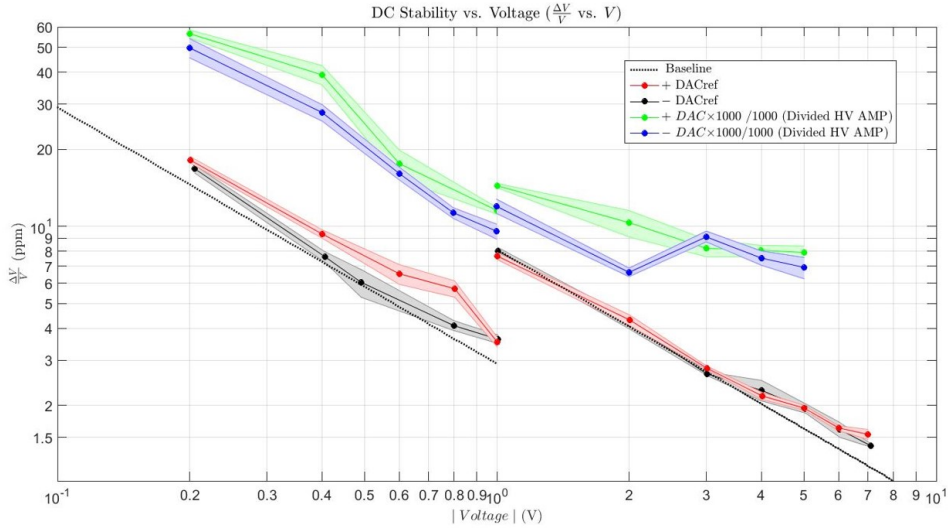

Figure 5.14: Plotted above is the DAC fractional stability and amplified DAC stability, measured in ppm, for different programmed output voltages. Data taken using a 1000× voltage divider using precision z-foil type resistors.

The drifts in high-voltage output motivates the need for a high-voltage control loop to ensure the high-voltage follows the desired low-voltage DAC signal.

5.1.4 High-Voltage Control Loop

Control loops are found in many AMO experiments, and are often referred to as servos. They can be used to stabilize lasers (frequency, phase, and intensity), temperature sensitive devices, magnetic fields, or any other signal where stability is required. Each high voltage source for our experiment will use a control loop in order to ensure the output voltage follows

the desired voltages set by the DACs. This requires the servo to accurately follow the DAC during the 1ms ramps that will be used in the experiment and settle to the required stability in a short time period.

Below, in Figure 5.15, is an image of the high-voltage divider and error amplifier board. Minimal error in these components is crucial in order to accurately compare the high voltage signal to the DAC signal. Any error introduced by these components reduces the servo's ability to follow the DAC. As a result, we use a high precision voltage divider comprised of 30 high-stability Vishay resistors (Z-foil type) that have an extremely low temperature coefficient of 0.05ppm/°C. Placing this number of resistors in series minimizes the voltage drop seen at each resistor which in turn reduces sensitivity to resistor error. Additionally, as with the op-amps chosen for the LM399 references, the error amplifier uses an ultralow noise op-amp to amplify the error signal. A capacitor in feedback is used to smooth variations in the error signal. This makes for what is known as an Integrating stage (I).

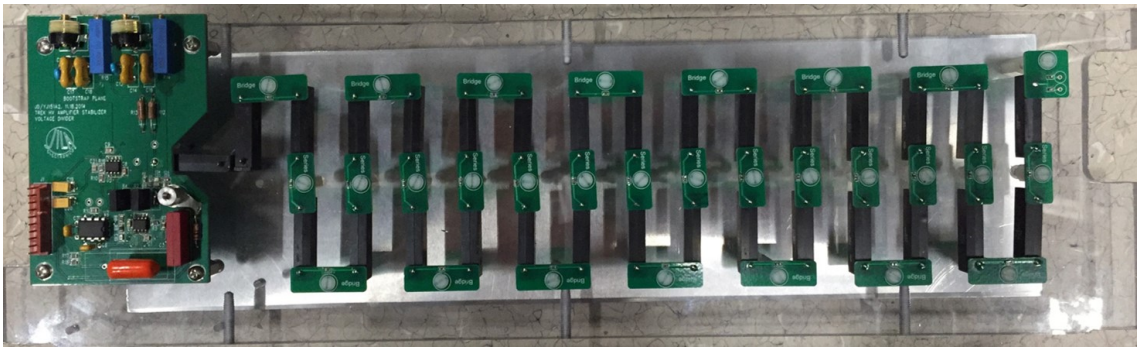

Figure 5.15: High-voltage divider and error amplifier board.

Following the error amplifier is the loop filter. It's job is to suppress the error signal so as to match high-voltage to DAC voltage. It must correct for any errors created by both the high-voltage amplifier and voltage divider and therefore must be capable of reducing error caused by voltage drift and noise as well as overshoot from the 1ms ramps to high-voltage. Requiring the high-voltage signal to be stable on the ppm level necessitates extremely large gain from the loop filter, at both low and high frequency ranges. We can talk about the gain

at each frequency range in terms of the different functions the loop filter components serve. The first component is a called Proportional Integrator (PI). Its function is to provide gain at low frequencies, correcting low frequency noise and long term drift. The gain of this component reduces at higher frequencies, demanding a second component with high frequency gain, called a Differentiator (D). This stage enables error reduction for high frequency noise as well as ramping overshoot. Following this component is another PI stage which provides more gain at low frequency for pushing the error down. In total, these components make for an I-PI-D-PI servo (schematics in Figures A.8 and A.9). Finally, the servo can further reduce overshoot by using feedforward.

The next image shows the servo fully built, with labels indicating each component. Because the voltage divider and error amplifier are most sensitive to error, they are placed separately from the loop filter board and shielded from external noise sources by two metal walls. Additionally, the warped metal plate (compensation plate) is used to extend the bandwidth of the servo. It does this by coupling signals back into the error amplifier board that have been lost due to capacitance between the resistors and surrounding metal box. Our control loop was designed by Terry Brown in JILA's electronics shop.

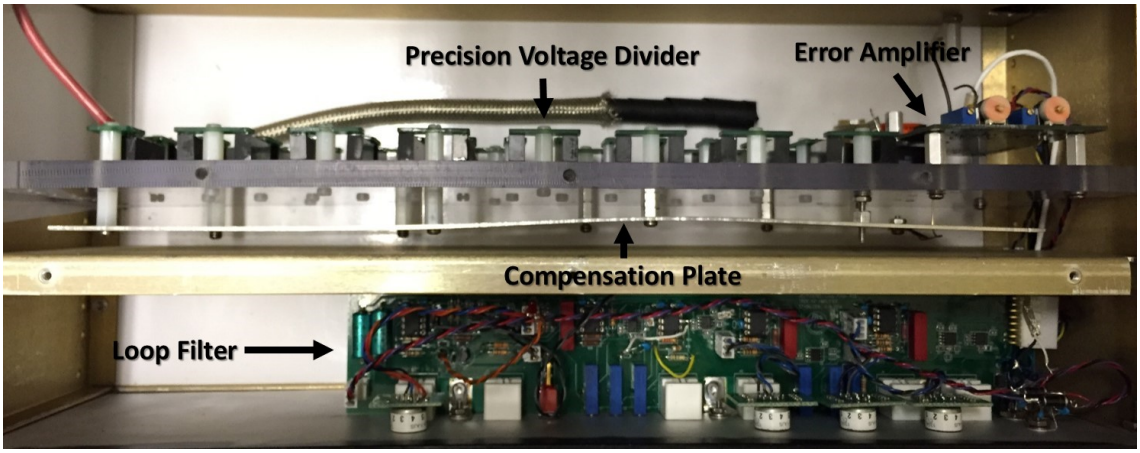

Figure 5.16: High-voltage control loop fully assembled. Component locations indicated by arrows. Error amplifier, voltage divider, and compensation plate are placed separately from the loop filter in order to reduce any source of error in the divided high-voltage signal.

After building the servo, we measured its ability to suppress error as a function of frequency. Below is plot showing the servo is capable of reducing error between the high voltage output and the desired DAC input by at least a factor of one million out to roughly 30Hz AC (when using feedforward). The data collected above for the DAC and high-voltage amplifier in Figure 5.14 shows a discrepancy between the two signals of at most a factor of two at DC. We believe the servo should have no trouble correcting this discrepancy.

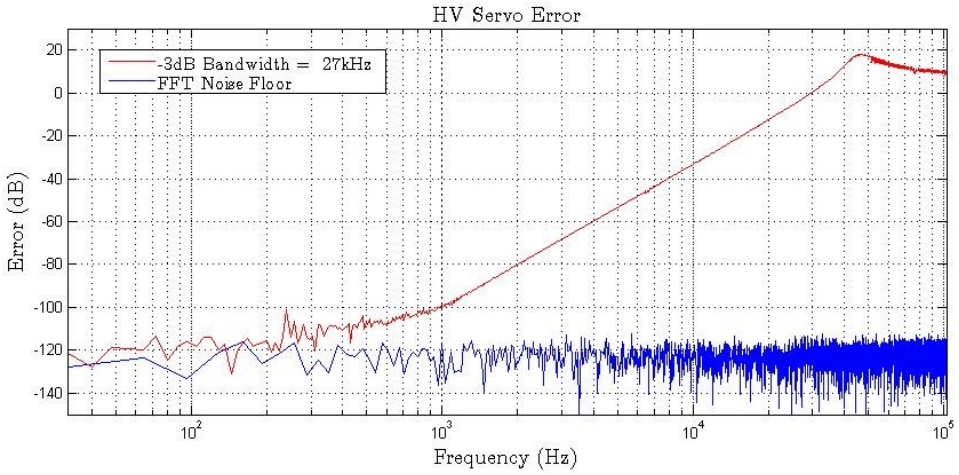

Figure 5.17: Error signal vs. frequency for high-voltage servo using feedforward. Data taken using the <F2/F1> feature of the SR780 FFT.

5.2 Conclusions

Thus far we have been able to measure the servo bandwidth and the stability over various time scales for the individual components of a single high-voltage source. If the servo performs as well as we expect, the high-voltage fractional stability should be below the targeted goal of 10ppm for AC noise and DC drift over 12hr windows. This will provide the repeatability necessary for taking long data sets. However, the dependence of stability on DAC voltage may require more consideration in order to achieve the levels of fractional stability needed at the average electric field strengths presented in Table 4.1.

Chapter 6

Future Outlook

Moving forward, we would like to measure the stability of the system as a whole. To begin with, we would like to retake data for fractional stability versus average voltage to demonstrate that the high-voltage servo is capable of matching the DAC stability for all possible high-voltage values. Additionally, we would like to measure the output noise of the amplifier as a function of voltage to determine the type of filtering necessary before the plates and rods. For future testing we have set up a mock test chamber that has two aluminum plates equal in size and spacing to those of the new science cell. This is shown below in Figure 6.1.

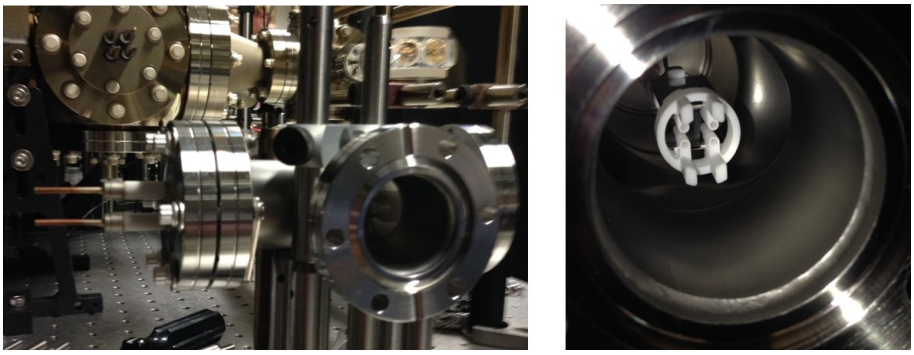

Figure 6.1: Mock chamber for testing high-voltage sources without risking damage to science cell. The chamber will be in vacuum with two viewing windows.

The mock test chamber should prove useful in verifying functionality of the final design without risking damage to the new science cell. However, there is ultimately not substitute

for measuring the molecules which are the ultimate test for electric field stability.

Bibliography

[1] C. E. Wieman E. A. Cornell. The bose-einstein condensate. Sci. Am., 278:40–45, 1998.

[2] DeMarc B. D. S. Jin. Onset of fermi degeneracy in a trapped atomic gas. Science, 285,5434:1703–1706, 1999.

[3] N. Goldman et al. Light-induced gauge fields for ultracold atoms. Rep. Prog. Phys, 77:126401, 2014.

[4] I. Bloch et al. Quantum simulations with ultracold quantum gases. Nature, 8:267–274, 2012.

[5] D. S. Jin J. Ye. Polar molecules in the quantum regime. Phys. Today, 64(5):31, 2011.

[6] L. D. Carr et al. Cold and ultracold molecules: science, technology, and applications. New Journal of Physics, 11:87, 2009.

[7] T. Lahaye et al. The physics of dipolar bosonic quantum gases. Rep. Prog. Phys., 11:87, 2009.

[8] M. L. Wall Ana Marie Rey, K. R. A. Hazzard. Quantum magnetism with ultracold molecules. Arxiv, June 2014.

[9] W. Klemperer et al. Can molecules have permanent electric dipole moments? J. Phys. Chem., 97:2413–2416, 1993.

[10] Kang-Kuen Ni. A Quantum Gas of Polar Molecules. PhD thesis, University of Colorado at Boulder, 2009.

[11] Joshua Zirbel. Ultracold Fermionic Feshbach Molecules. PhD thesis, University of Colorado at Boulder, 2008.

[12] K.-K. Ni et al. Dipolar collisions of polar molecules in the quantum regime. Nature, 464:1324–1328, 2010.

[13] M. H. G. de Miranda et al. Controlling the quantum stereodynamics of ultracold bimolecular reactions. Nature, 7:502–507, 2011.

[14] A. Chotia et al. Long-lived dipolar molecules and feshbach molecules in a 3d optical lattice. Phys. Rev. Lett., 108:080405, 2012.

[15] B. Yan et al. Observation of dipolar spin-exchange interactions with lattice-confined polar molecules. Nature, 501:521–526, 2013.

[16] W. Ketterle N. J. Van Druten. Evaporative cooling of trapped atoms. Advances in atomic, molecular, and optics physics, 37:181–231, 1996.

[17] S. V. Syzranov et al. Spin-orbital dynamics in a system of polar molecules. Nature Comms., 5:1–7, 2014.

[18] M. H. S. Amin. Rabi oscillations in systems with small anharmonicity. Arxiv, July 2004.

[19] K.-K. Ni et al. A high phase-space density gas of polar molecules. Science, 332:231–235, 1996.

[20] H.-C. Nagerl et al. A high phase-space density gas of polar molecules. J. Phys.:Conf. Ser., 264, 2011.

[21] W. Li et al. A homonuclear molecule with a permanent electric dipole moment. Science, 334:1110–1114, 2011.

[22] A. Zaitsevskii et al. Permanent electric dipoles and λ-doubling in the lowest π-states of rbcs. Phys. Rev. A, 71:1–6, 2005.

[23] A. Zaitsevskii et al. Evaporative cooling of reactive polar molecules confined in a two-dimensional geometry. Phys. Rev. A, 88:063405, 2013.

[24] Yan et al. Observation of dipolar spin-exchange with lattice-confined polar molecules. Nature, 501:521–525, 2013.

Appendix A

Additional Information for High-Voltage Design

A.1 ±Voltage References

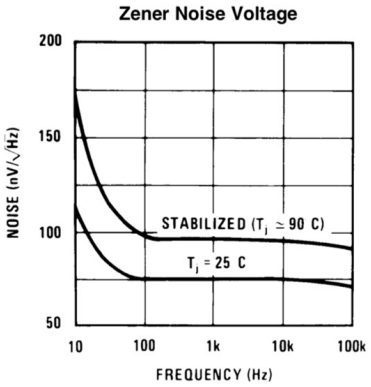

Figure A.1: LM399 noise spectrum.

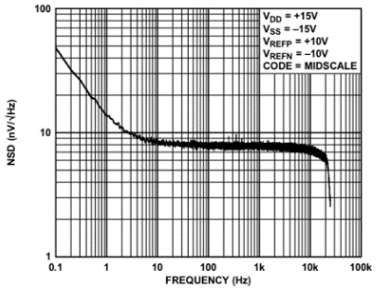

Figure A.2: DAC (AD5791) noise spectrum.

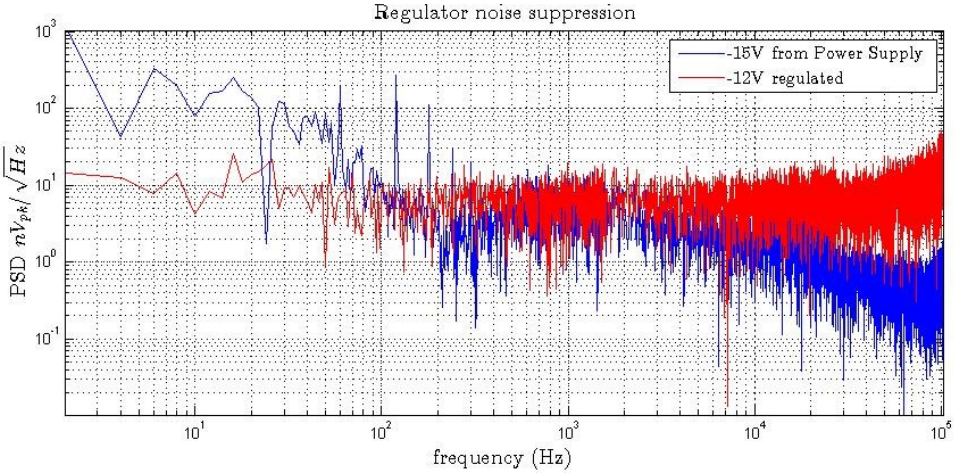

Figure A.3: Comparison of voltage noise from power supply with and without -12V regulator. We believe this is the cause of the increasing noise at high frequencies in reference circuit.

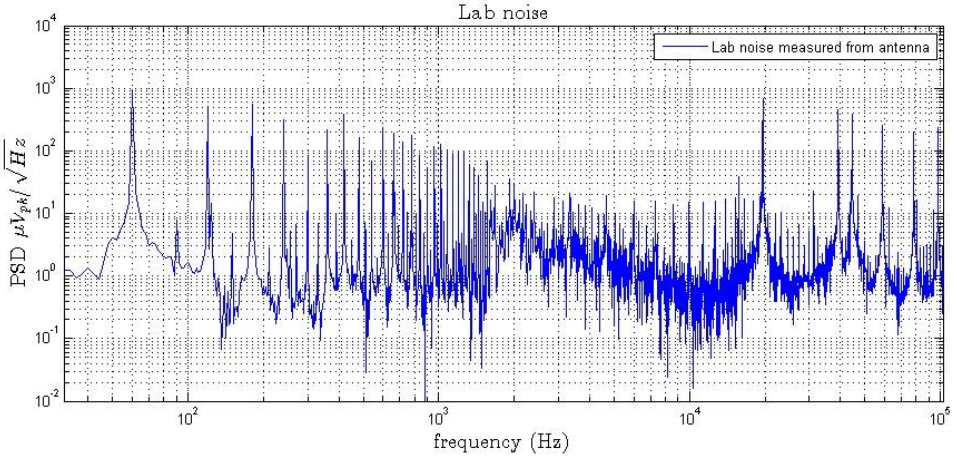

Figure A.4: Noise spectrum measured in the KRb lab with antenna using SR780 FFT.

A.2 High-Voltage

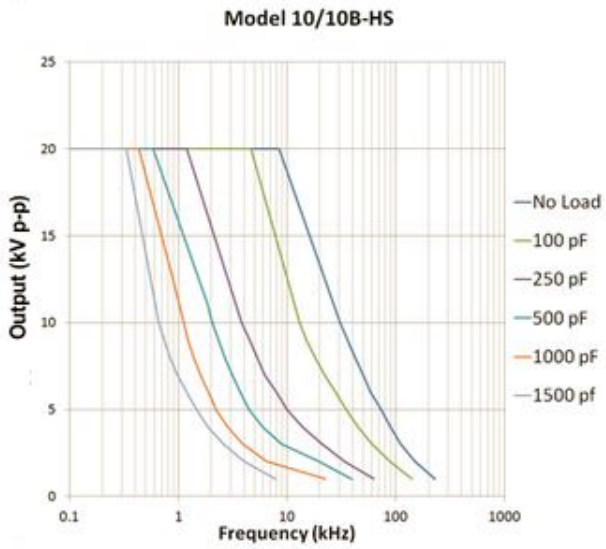

Figure A.5: Bandwidth of Trek high-voltage amplifier.

A.2.1 Reference Schematics

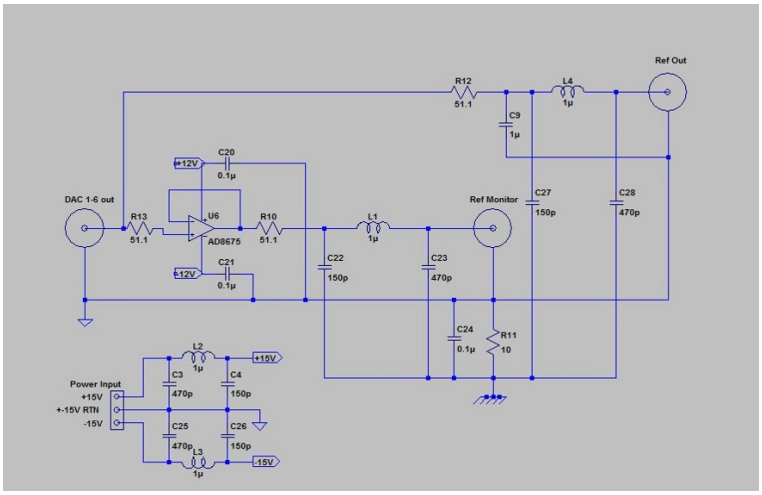

Figure A.6: Filter diagrams for all inputs and outputs of the DAC box.

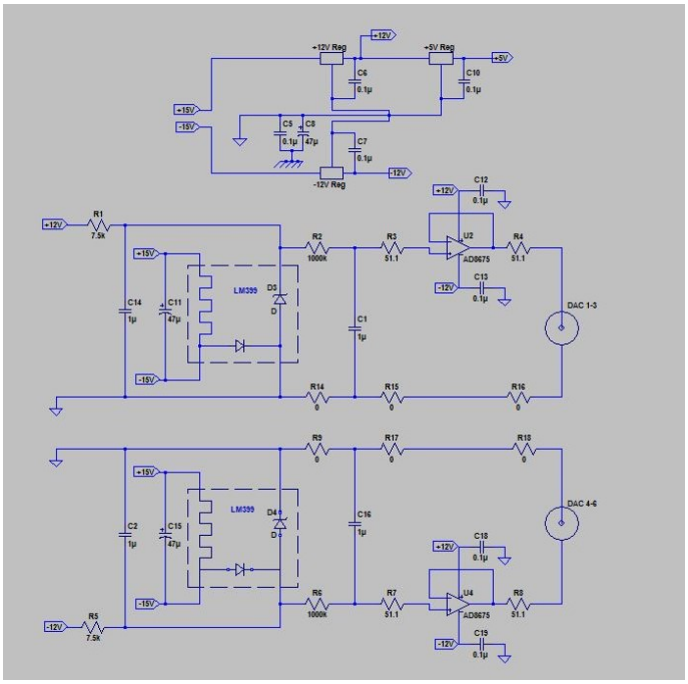

Figure A.7: ±LM399 and power input circuit diagrams.

A.2.2 Servo Schematics

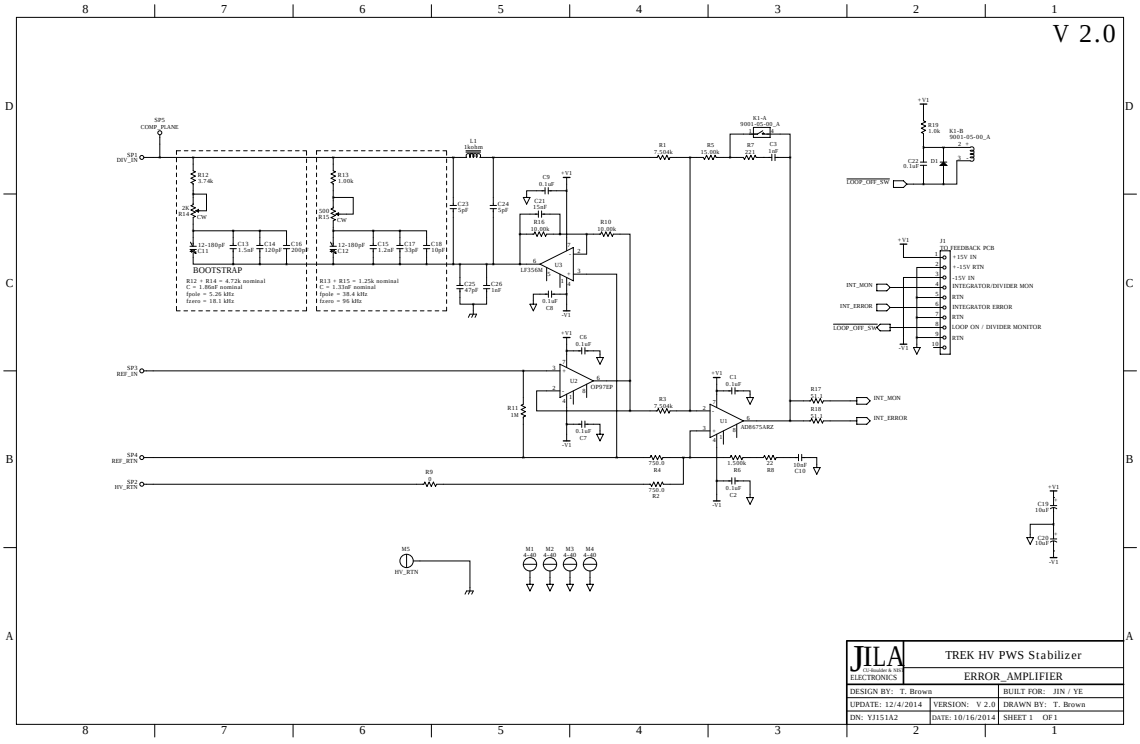

Figure A.8: Error amplifier circuit diagram.

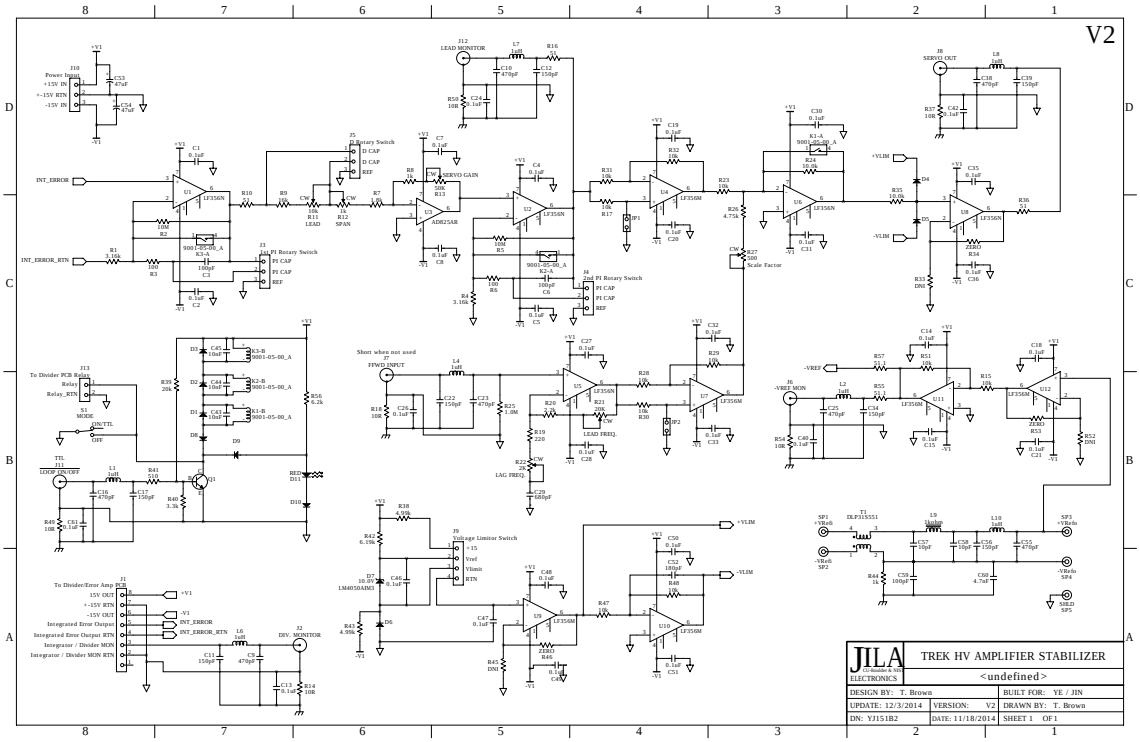

Figure A.9: Loop filter circuit diagram.